2D Materials

OPEN ACCESS

RECEIVED
22 February 2018

REVISED
10 April 2018

ACCEPTED FOR PUBLICATION
26 April 2018

PUBLISHED
11 May 2018

PAPER

A blueprint for the synthesis and characterisation of thin graphene oxide with controlled lateral dimensions for biomedicine

Artur Filipe Rodrigues[1], Leon Newman[1], Neus Lozano[1], Sourav P Mukherjee[2], Bengt Fadeel[2], Cyrill Bussy[1] and Kostas Kostarelos[1]

[1] Nanomedicine Lab, Faculty of Biology, Medicine and Health and National Graphene Institute, The University of Manchester, Manchester, United Kingdom

[2] Nanosafety and Nanomedicine Laboratory, Institute of Environmental Medicine, Karolinska Institutet, 17177 Stockholm, Sweden

E-mail: cyrill.bussy@manchester.ac.uk **or** kostas.kostarelos@manchester.ac.uk

Keywords: graphene, graphene oxide, characterisation, standardisation, 2D materials, endotoxin free, non pyrogenic, nanomaterials

Supplementary material for this article is available online

Abstract

Graphene-based materials (GBMs) have ignited a revolution in material science and technology, with electronic, optical and mechanical properties that are of relevant interest for a wide range of applications. To support the development of these enabling technologies, a global research effort has been invested to assess their hazard and biocompatibility. Different production methods have however generated a diverse collection of GBMs with different physicochemical properties, leading to a variety of biological outcomes that are still not fully understood. To better understand the biological interactions of GBMs with biological systems and allow the design of safer materials, a thorough physicochemical characterisation is therefore highly recommended. The aim of the present work was to produce a blueprint for the synthesis and characterisation of non-pyrogenic graphene oxide (GO) flakes with three different controlled lateral dimensions, which could be further used for either hazard assessment or biomedical proof-of-concept studies. A battery of techniques used to characterise the physicochemical properties of the GO samples included atomic force microscopy, transmission electron microscopy, Fourier-transformed infra-red spectroscopy, x-ray photoelectron spectroscopy and Raman spectroscopy. The combination of these different techniques confirmed that only the lateral dimension varied among the GO materials produced, without significant change in any other of their fundamental physicochemical properties, such as the thickness or surface chemistry. The proposed systematic approach in GO batch production for biology will hopefully contribute to a better understanding of the material properties that govern their interactions with biological systems and offer a blueprint towards standardisation of biologically relevant 2D materials.

Introduction

Graphene is a 2D material made of a monolayer of sp^2-hybridised carbon atoms organised as a hexagonal lattice [1, 2]. The discovery of some of its properties in 2004 represented an unprecedented breakthrough in fundamental physics, which was recognised with the attribution of the Nobel Prize in Physics in 2010 [3]. The enthusiasm generated by its unique combination of structural, mechanical, optical and electronic properties has quickly spread across a variety of scientific disciplines including physics, chemistry, material sciences and more recently biomedical sciences [2, 4]. As a result, a variety of scalable production methods have been developed to overcome the low throughput of the original micromechanical exfoliation of graphite layers down to single-layer graphene, including chemical vapour deposition (CVD) and liquid phase exfoliation of graphite in low surface energy solvents [2]. Such a variety led to the rise of a whole family of graphene-based 2D materials (GBMs), exhibiting various structural and physicochemical properties [5, 6].

Graphene oxide (GO) is a prominent GBM, which can be easily produced by oxidation and exfoliation of graphite under acidic conditions. This exfoliation of graphite yields graphene flakes that are decorated with a large amount of oxygen functional groups including

epoxides, hydroxyls and carboxyls [7]. Due to this specific surface chemistry, GO flakes present interesting features for biological and biomedical applications, including both a high colloidal stability in physiological *milieu* compared to pristine graphene, and an extremely high surface area-to-volume ratio that enables interactions with a wide range of molecules [2, 8]. GO can also be chemically modified in numerous ways, providing an attractive playground for medicinal chemists to anchor a variety of therapeutic molecules or imaging probes for biomedical purposes, or to tune the biological properties of GBMs themselves [7, 9, 10]. Together with its favourable size-dependent pharmacokinetics and urinary excretion [11, 12] and its biocompatibility [13, 14], GO has raised considerable interest in nanomedicine for its use as a nanovector [2, 8, 9, 15].

However, there are still concerns regarding the safety of GO and other GBMs. These concerns have been met with numerous but unfortunately contradictory reports on the materials' biological impact [16–18]. Such confounding information has hindered the comparison between nanosafety studies, due to an insufficient physicochemical characterisation of the tested GBMs [5, 16, 18]. A detailed characterisation methodology is highly desired to establish correlations between specific properties of GBMs (such as lateral dimensions and surface chemistry) and their biological activity. A better understanding of this relationship would ultimately facilitate the predictions of their potential health risks and allow for more informed decisions to be made regarding the translation of these materials from the lab bench to the clinic [19, 20]. In order to establish such correlations, GBMs with controlled physicochemical properties should be synthesised so individual variables can be tested. Moreover, the development of facile production methods of non-pyrogenic (endotoxin-free) GBMs, especially GO, with reproducible, high-standard dimensional features, defined functionalisation degree, and high chemical purity represents a key endeavour for their use in nanomedicine, as well as hazard assessment studies.

Here, we report the synthesis of three different aqueous dispersions of non-pyrogenic, few-layer GO sheets, varying only by their lateral dimensions. These dispersions were subjected to a thorough characterisation of their morphology, including lateral dimensions and thickness, and their surface properties, focusing on their chemical composition, in order to describe their properties according to referential classification frameworks [5, 6]. The combination of multiple techniques helped minimise any bias in the analysis of the physicochemical properties of these GO materials.

Experimental

Chemical production of non-pyrogenic graphene oxide with controlled lateral dimensions

Graphite flakes (Nacional de Grafite Ltda, Brazil) were used as the starting material to prepare graphene oxide by the modified Hummers' method as previously described [22]. While endotoxin-free water (water for injections) was acquired from Fresenius Kabi Ltd., UK, all other reagents were purchased from Merck-Sigma Aldrich, UK. All glassware and instruments used for the reaction were previously washed with 35% nitric acid (HNO_3) and left to dry for at least 4 h in the oven at 180 °C, as a depyrogenation step. All steps were performed in a non-pyrogenic environment, which involved the minimisation of potential contamination by using depyrogenated glassware and water for injections, and handling the GO dispersions only under horizontal laminar flow cabinets.

A mixture containing 0.8 g of graphite flakes and 0.4 g of sodium nitrate ($NaNO_3$) was prepared in a round-bottom flask placed on an ice bath, which was positioned on top of a magnetic stirrer. A volume of 18.4 ml of 99% sulfuric acid (H_2SO_4) was gradually added to the mixture whilst slightly increasing the stirring speed. After the mixture was left to stir for 10 min, 2.4 g of potassium permanganate ($KMnO_4$) were added very slowly. The ice bath was replaced by a distilled water bath, which allowed the temperature of the reaction to increase gradually over time. After 30 min, the mixture was more homogenous and became a thick, dark green paste, into which 37.5 ml of water for injections were transferred very slowly, drop by drop using a sterilised glass Pasteur pipette (Fisher Scientific, UK). During this procedure, a violent purple effervescence was observed as a result of the reaction between the water and the acidic mixture, followed by a sharp increase in temperature. Then, the water bath was replaced by an oil bath that was pre-heated at 80 °C–90 °C, so that the reaction temperature could stabilise at 98 °C, not exceeding 100 °C owing to a temperature controller. The mixture was kept stirring for 30 min and started displaying a thicker, paste-like appearance of a dark brown/green colour, which indicated the oxidation of graphite. Then, 112.5 ml of warm water for injections (T ~ 50 °C) followed by 12.5 ml of 30% hydrogen peroxide (H_2O_2) were finally added in order to stop the reaction, by reducing the residual $KMnO_4$, manganese dioxide (MnO_2) and dimanganese heptoxide (Mn_2O_7) to soluble manganese sulfate ($MnSO_4$) salts [7]. Effervescence could be observed as a result of the release of carbon dioxide (CO_2), confirming the termination of the reaction. The round-bottom flask was covered with aluminium foil and left to rest for 1 h.

The resulting dispersion was then homogenised and transferred into four sterile 50 ml centrifuge tubes, which were vortexed for a few seconds at maximum speed and centrifuged at 9000 rpm for 20 min. The supernatant was discarded, but its pH was measured. The graphitic pellet was then re-dispersed in fresh water for injections and the centrifugation steps were repeated multiple times (usually about 6 cycles) until a neutral pH was obtained in the supernatant. This was also characterised by the formation of an orange, gel-like layer at the interface between the pellet and

the supernatant. Details regarding the temperature conditions of the different centrifuge cycles as well as vortex duration time were provided in a previous publication from our group [22]. Mechanical exfoliation of GO was performed by vortexing for 5 min at maximum speed, followed by centrifugation, which led to the accumulation of thin GO flakes on top of the black graphitic debris. The orange layer was then solubilised in warm water for injections and carefully collected while avoiding remixing with the pellet. Eventually, a brownish aqueous solution containing highly dispersible, large graphene oxide flakes (l-GO) was obtained. The remaining graphitic impurities were removed 24 h post-reaction after an ultimate centrifugation cycle at 9000 rpm for 20 min at 20 °C. GO was freeze-dried for 3 d, in order to estimate the concentration of l-GO before reconstituting in the same volume of water for injections to perform sonication.

Small GO flakes (s-GO) were produced from reconstituted l-GO dispersion by exposing aliquots that were dispensed to depyrogenated and autoclaved glass vials to a water bath sonicator (VWR, UK) operating at 80 W (45 kHz) for 5 min. The dispersion was then centrifuged at 13 000 rpm for 5 min in order to remove the remaining l-GO flakes. Ultrasmall GO flakes (us-GO) were produced from the l-GO dispersion and were processed in a similar manner, adjusting the sonication time to 4 h and the centrifugation time to 1 h. In this latter case, the water level in the sonication bath was regularly adjusted and its temperature carefully monitored so that it did not exceed 40 °C; the water bath was replaced approximately every hour. The concentration of these 2 materials was also determined by comparing the sample weight before and after freeze-drying 20 ml of each dispersion.

Optical microscopy

Samples were prepared on 12-well plates by depositing on each well 1 ml of a GO dispersion diluted in Milli-Q ultrapure water (Merck Millipore, UK) to a concentration of 20 μg ml^{-1}. After allowing the flakes to sediment for 24 h at room temperature, the samples were observed using a PrimoVert inverted microscope (Carl Zeiss, UK) in bright-field at a magnification of 200×. Only micrometre-sized flakes were visible under the optical microscope, which resulted in the recording of images of l-GO only. Hundreds of flakes were manually measured on ImageJ (version 1.49, NIH, USA) by determining the longest Feret diameter in each object.

Transmission electron microscopy

TEM was performed using a BioTwin electron microscope (Philips/FEI, Netherlands), Technai 12 instrument operated at an accelerating voltage of 100 kV, a spot size of 1 and an aperture size of 3. The beam exposure time was 0.1 s whereas the camera exposure time was set to 1 s. Both 1900× and 4800 × magnifications were used to image l-GO and s-GO, whereas us-GO samples were analysed using the 6800× magnification. Ten μl of sample were deposited on a carbon coated grid and filter paper was used to remove any excess of material after 1 min of deposition time. Carbon grids with the deposited l-GO samples underwent a prior glow discharge treatment. Lateral size distribution was carried out by manual counting on ImageJ software on several TEM images.

Atomic force microscopy

Samples were prepared after depositing 20 μl of GO dispersion (100 μg ml^{-1}) on a freshly cleaved mica surface (Agar Scientific, UK) coated with 20 μl of 0.01% poly-L-lysine (Sigma-Aldrich, UK) and allowed to adsorb for 2 min. Excess of materials was then removed by rinsing with Milli-Q ultrapure water (Merck Millipore, UK). Samples were left to dry overnight at 37 °C in a drying cabinet.

AFM images were acquired in air using a Multimode 8 atomic force microscope (Bruker, UK) in tapping mode using OTESPA tips (Bruker, UK) of 10 nm curvature radius, mounted on a tapping mode silicon cantilever with a typical resonant frequency of 300 kHz and a spring constant of 42 N m^{-1}.

Images were processed on Nanoscope Analysis software (version 1.4, Bruker, UK) and exported for further background removal and particle analysis on ImageJ, using a segmentation algorithm. Values obtained for lateral dimensions and thickness were used for the boxplots and statistical analysis.

Fluorescence spectroscopy

Fluorescence emission spectra were acquired for a range of GO dispersions prepared with different concentrations (25–200 μg ml^{-1}), using a Cary Eclipse fluorescence spectrophotometer (Varian Inc., Agilent Technologies, UK). Measurements were performed at room temperature, using $\lambda_{exc.} = 525$ nm, with both excitation and emission slits defined at 20 nm.

UV/visible spectroscopy

Absorbance spectra were acquired after diluting the GO samples prepared for fluorescence measurements by a factor of 10 in water (2.5–20 μg ml^{-1}), using a Cary 50 Bio UV/Vis spectrophotometer (Varian Inc., Agilent Technologies, UK). These samples were transferred to a 1 ml quartz cuvette with 1 cm path length. Measurements were performed at room temperature, using a dual beam mode with baseline correction based on water as a blank control.

Raman spectroscopy

GO samples were prepared in duplicate by drop casting 20 μl of GO dispersed in water (100 μg ml^{-1}) onto a borosilicate glass slide. Samples were left to dry for at least 2 h at 37 °C in a drying cabinet. Measurements were carried out using a DXR microRaman spectrometer (Thermo Scientific, UK) with a 50× objective.

In each measurement, samples were irradiated for 25 s with a laser of $\lambda = 633$ nm with a power of 0.4 mW and a 50 μm pinhole aperture. Five different locations were measured, and five measurements were performed for each location. Data processing implied baseline correction and normalisation of the Raman scattering intensity according to the G band, allowing the quantification of the formation of defects in the graphene lattice through the calculation of the I_D/I_G ratio.

Zeta potential measurements

Electrophoretic mobility (μ) was measured using a ZetaSizer Nano ZS (Malvern Instruments, UK) after dilution of GO with water to a concentration 20 μg ml^{-1}, in disposable ZetaSizer cuvettes (Malvern Instruments, UK). Default settings and automatic analysis were used for all measurements, where the μ value was converted automatically by the equipment software to zeta potential (ζ) values according to Henry's equation. Each measurement was performed in triplicate at room temperature and values were reported as mean $\pm$ SD.

Fourier transform infrared spectroscopy

Fourier transform infrared spectra were obtained with a Tensor 27 spectrometer (Bruker, UK), equipped with a 3000 Series High Stability Temperature Controller with RS232 Control (Specac, UK) and a MKII Golden Gate Single Reflection ATR system (Specac, UK) for measurements in ATR mode. The bottom plate of the Golden Gate ATR system was pre-heated at 60 °C to allow the complete evaporation of water from the drops (typically 20 μl) of the original GO dispersions. About 3 min after depositing the dispersions on the plate, the transmittance spectra of GO were recorded by acquiring 32 scans in the 4000–700 cm^{-1} range, with a resolution of 4 cm^{-1}.

Thermal gravimetric analysis

Lyophilised GO samples (~2 mg) were weighed into a ceramic crucible. Measurements were performed using a TGA 4000 thermogravimetric analyser (PerkinElmer Ltd, UK) from 25 °C to 995 °C at a rate of 10 °C min^{-1}. Nitrogen at a flow rate of 20 ml min^{-1} was used as a purge gas. Once a temperature of 995 °C was reached, gas supply was switched to oxygen for 15 min in order to burn the remaining material.

X-ray photoelectron spectroscopy

Lyophilised GO samples were sent to the National EPSRC XPS Users' Service (NEXUS) facility, hosted by nanoLAB at Newcastle University, for XPS measurements. XPS was recorded using a Thermo Theta Probe XPS spectrometer with a monochromatic Al K-α source of 1486.68 eV. The survey XPS spectra were acquired with pass energy (PE) of 200 eV, 1 eV step size, 50 ms dwell time and averaged over 5 scans. The etching was 90 s. The high resolution C1s XPS spectra were acquired with PE of 40 eV, 0.1 eV step size, 100 ms dwell time and averaged over 20 scans.

Spectra were processed using CasaXPS software (Casa Software Ltd, UK). The contribution of charge injected to insulating samples was corrected by calibrating all peaks according to the adventitious carbon C1s spectral component, set at a binding energy of 284.6 eV. Deconvolution of high-resolution C1s and O1s spectra were performed after a Shirley background subtraction. Gaussian–Lorentzian (70:30) functions were fitted to all identified functional groups. Due to its asymmetric nature, the graphitic peak corresponding to C–C and C=C bonds was fitted using an asymmetric Lorentzian function. All deconvoluted peaks, apart from the π–π^* contribution, had their full width half maximum value constrained between 0.5 and 2 eV. Identified functionalities had also their peaks constrained to the following binding energies, according to NIST's XPS and la surface databases:

- π–π^*: 290.0–292.0 eV
- O–C=O: 288.6–290.0 eV (C1s); 533.0–534.0 eV (O1s)
- C=O: 286.8–287.8 eV (C1s); 530–531.5 eV (O1s)
- C–O: 285.5–286.6 eV (C1s); 532.0–533.0 eV (O1s)
- C–C and C=C: 284.5–284.6 eV

Endotoxin assessment using TNF-α expression test (TET)

The TNF-α expression test (TET) enables unequivocal detection of endotoxin in graphene-based materials with a sensitivity that is comparable to the conventional LAL assay, but without any interference with the assay [23]. In brief, the TET assay comprises of two steps: (i) cytotoxicity testing of the material (e.g. Alamar Blue assay) to determine a dose that is non-cytotoxic for HMDM; (ii) measuring TNF-α secretion after exposure of HMDM to the test material at a non-cytotoxic dose, using a commercially available ELISA.

Isolation of primary human macrophages

Peripheral blood mononuclear cells (PBMC) were isolated from buffy coats obtained from healthy human blood donors (Karolinska University Hospital, Stockholm, Sweden) by density gradient centrifugation, as described previously [71]. Then, the PBMCs were positively selected for CD14 expression using CD14 MicroBeads (Miltenyi Biotech Ltd, Bergisch Gladbach, Germany). To obtain human monocyte-derived macrophages (HMDM), CD14+ monocytes were cultured in RPMI-1640 cell medium supplemented with 2 mM L-glutamine, 100 IU ml^{-1} penicillin, 100 μg ml^{-1} streptomycin, and 10% heat inactivated FBS, supplemented with 50 ng ml^{-1} recombinant M-CSF for three days in 96 well plates.

Cell viability assay

HMDMs were exposed to GOs up to 75 μg ml^{-1} in RPMI-1640 medium supplemented with 10% FBS (without M-CSF) in parallel to 5% DMSO as a positive control for cell death for 24 h. Then, the Alamar Blue (AB) assay was performed according to the manufacturer's instruction. Briefly, medium was removed, cells were rinsed with PBS and 100 μl of AB medium (5% (v/v) solution of AlamarBlue® reagent), prepared freshly in RPMI-1640 medium, were added to each well. After 2 h of incubation at 37 °C, fluorescence was measured using a Tecan Infinite F200 plate reader. The experiment was performed with at least six replicates for each concentration of GO. Results were expressed as % cell viability versus control. Potential interference with the assay was evaluated in an acellular system by incubating 75 μg ml^{-1} of each of the GOs with the AB reagent for 2 h at 37 °C.

TNF-α measurement by ELISA

HMDMs were incubated with GOs at 50 μg ml^{-1} concentrations in the presence or absence of LPS inhibitor polymyxin B sulfate (10 μM) for 24 h in complete RPMI medium supplemented with 10% FBS [23]. LPS dose response (0.1–100 ng ml^{-1}) was included as a positive control. Following exposure, cell culture supernatants were collected and the secretion of TNF-α was determined by ELISA according to the manufacturer's instruction (MABTECH, Nacka Strand, Sweden). The difference between the TNF-α expression induced by GOs with or without Poly-B corresponds to the endotoxin present in the sample.

Statistical analysis

All experiments were repeated at least twice. Due to different sample sizes and the non-Gaussian distribution of the flake populations, the size distribution data was presented using boxplots and the median, minimum and maximum values of each distribution were reported. A non-parametric test (Wilcoxon rank sum test) was performed using the statistical package in MATLAB (version R2013a, MathWorks Inc., USA), in order to study the statistical significance of the difference between the groups in terms of lateral dimensions.

Contributions of functional groups in high-resolution C1s and O1s XPS of GO samples were compared by a non-parametric Kruskal–Wallis test. A reported p-value <0.05 was considered for *post hoc* Dunn's multiple comparison tests, in order to confirm the differences in the surface chemistry among the three materials. At least four replicates were used for each exposure condition. One-way ANOVA with post-hoc Turkey's test between groups with and without polymyxin B sulfate was performed in the TET assay. Differences among mean values were considered significant when p-value <0.05. Statistical analysis was performed using GraphPad Prism software (version 6.01, GraphPad Inc., USA).

Results

Synthesis of high-purity graphene oxide flakes with controlled lateral dimensions

GO was prepared after oxidation of graphite flakes using a modified version of the Hummers' method, under endotoxin-free conditions, as described previously by our group and summarised in figure 1 [21–23]. In order to maintain endotoxin-free conditions throughout the process, we took various precautions which included the depyrogenation of all used glassware, the use of disposable sterilised consumables and non-pyrogenic water for the chemical reaction steps, and the handling of GO dispersion under a horizontal laminar flow cabinet, as described in [23]. This procedure in its totality has been described in the experimental section.

The resulting graphite oxide dispersion underwent multiple centrifugation rounds, followed by the removal of a liquid supernatant containing chemical impurities or contaminants such as residual potassium permanganate, fulvic acids and other metallic species. The graphitic pellet was re-dispersed in sterile, endotoxin-free water before each centrifugation step, until the supernatant's pH was neutralised (pH ~ 7). As a result, the supernatant became also less turbid, progressively changing from an originally translucent dark yellow to a more transparent state. The graphitic pellet was then re-dispersed and vigorously exfoliated by vortexing at maximum speed for 5 min. After another centrifugation round, a dark orange/brown, gel-like layer containing the desired thin GO sheets was present on top of black by-products, mainly composed of thick graphitic and oxidised graphite materials (figure 1(A)). This layer could be carefully extracted with warm water, avoiding the contamination of the product with unwanted graphitic impurities from the pellet. After repeating this process with a new centrifugation round, a final centrifugation step was performed on the extracted GO 24 h post-reaction in order to confirm the purification of large GO flakes (l-GO) as the end product, by removing any graphitic impurities that might have been extracted in the previous step (figure 1(B), blue arrows). The final yield of the reaction was relatively low, corresponding in mass to ~9% (w/w) of the starting graphite.

As described in figure 1 and detailed in the experimental section, a portion of the purified l-GO dispersion was freeze-dried and weighed to determine its mass-based concentration, before reconstituting with endotoxin-free water to the original volume. This reconstituted dispersion was then split in 2 post-reaction treatment groups to be further processed in order to reduce the size of the sheets: (i) exposure of l-GO to a sonication bath for 5 min followed by a

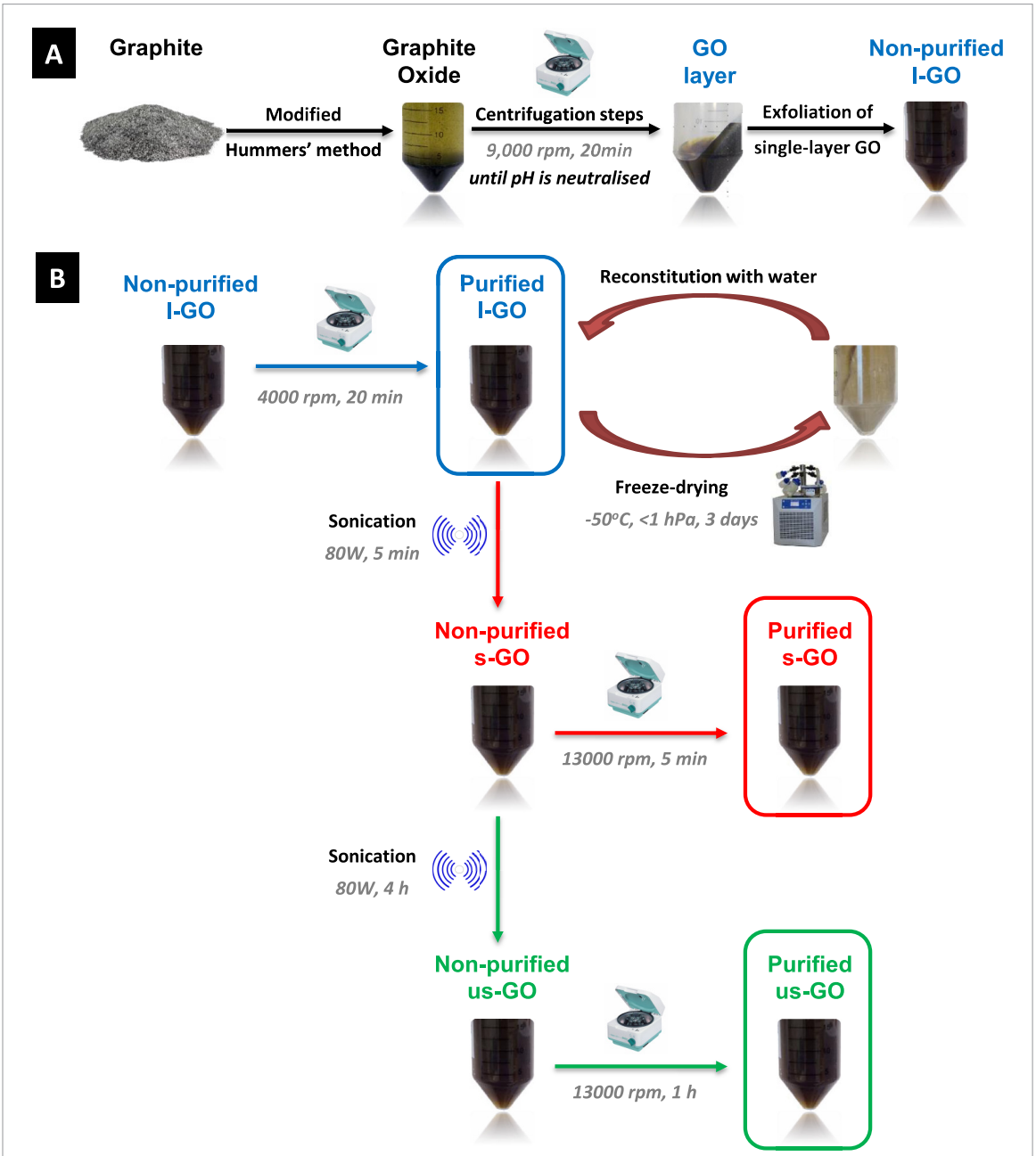

Figure 1. Synthesis of GO flakes of three different lateral dimensions. (A) Oxidation of graphite using the modified Hummers' method followed by mechanical exfoliation of graphene oxide. (B) Post-treatment steps for the preparation of l-GO (blue), s-GO (red) and us-GO (green).

centrifugal purification step to separate the small GO flakes (s-GO) from the larger flakes that deposited and formed a pellet (figure 1(B), red arrows); (ii) exposure of the aforementioned sonicated l-GO dispersions (without purification) to a sonication bath for an additional period of 4 h, followed by a centrifugal purification step to enable the extraction of purified ultrasmall GO flakes (us-GO) in the supernatant (figure 1(B), green arrows). In both cases, the temperature of the water bath employed in the sonication steps was controlled so that it did not exceed 40 °C (see experimental section). As demonstrated in the following sections, this method of production resulted in the acquisition of three types of GO flakes, which differed only by their lateral dimensions whilst displaying a conserved surface chemistry (see below). The production yield of s-GO and us-GO corresponded to ~90% (w/w) of the starting l-GO dispersion.

Structural properties and assessment of lateral dimensions

The morphology of the GO flakes was studied using optical microscopy, transmission electron microscopy (TEM) and atomic force microscopy (AFM) in a complementary fashion, and is presented in figure 2. In addition, a boxplot presentation of the measured lateral dimensions together with the respective number of analysed particles and statistical analysis is reported

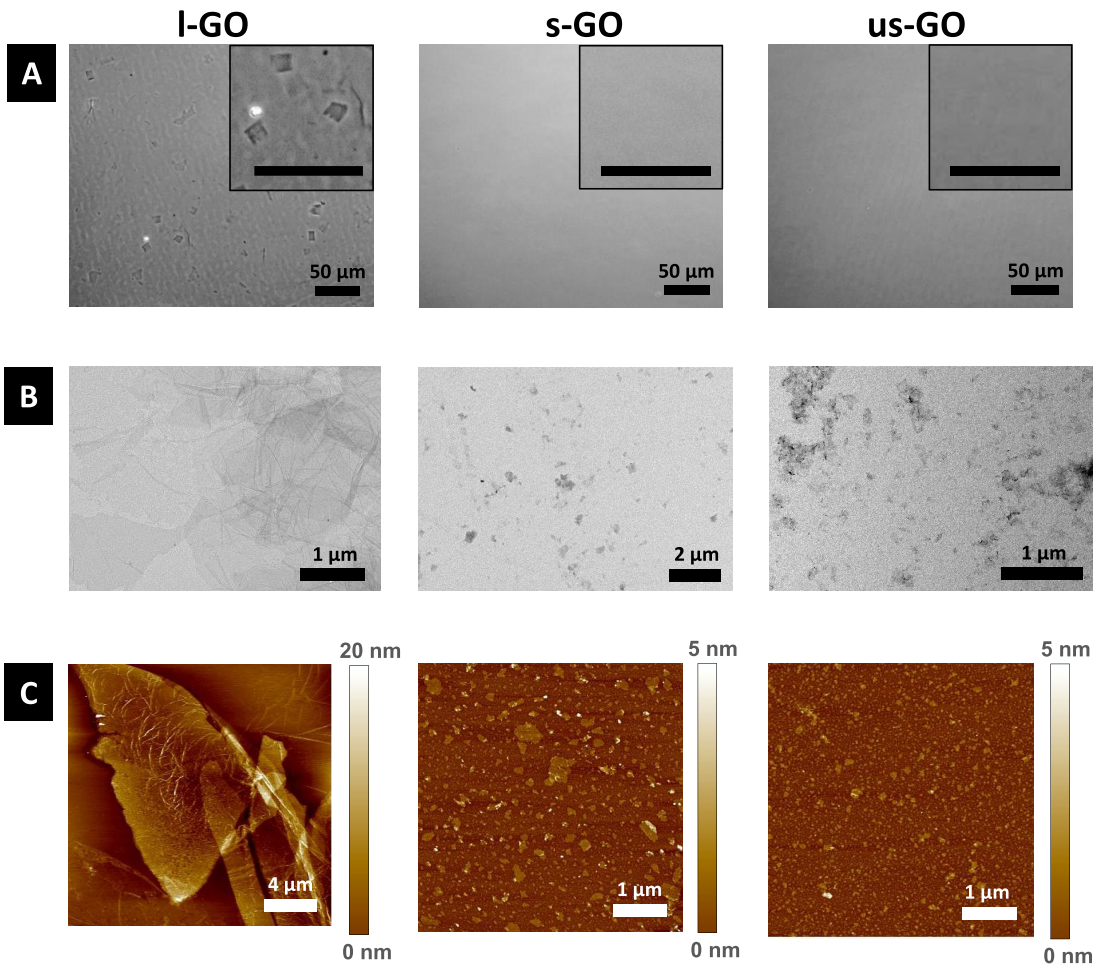

Figure 2. Structural observation of l-GO, s-GO and us-GO using different imaging techniques: optical micrographs (A); TEM micrographs (B); AFM height images (C). Only l-GO were visible under the optical microscope, suggesting that s-GO and us-GO had lateral dimensions below 1 μm.

in figure 3. Finally, the size distribution values (mean, minimum and maximum values) are summarised for each material in table S1 (supporting information (stacks.iop.org/TDM/5/035020/mmedia)) to support the comparison among the three GO types.

No particles were visible under the optical microscope in the case of s-GO and us-GO (figures 2(A) and 3(A)), confirming the production of materials smaller than the optical microscopy diffraction limit (Abbe's law). In contrast, in the l-GO sample, particles with lateral dimensions above 1 μm were clearly visible (table S1, supporting information). TEM micrographs showed a clear difference in lateral dimensions among the three materials (figure 2(B)). This was proven to be statistically significant ($p < 0.001$) after performing the Wilcoxon rank sum test (figure 3(B)), as the lateral dimensions of l-GO were an order of magnitude greater than the lateral dimensions of s-GO. The lateral dimensions of us-GO were approximately 5 times inferior than those of s-GO, reflecting a clear reduction in size compared to l-GO. Accordingly, the statistical analysis of the AFM scan dataset uncovered a clear statistical difference between l-GO and the other two sample groups ($p < 0.001$). However, while the images reflect a clear difference in lateral dimensions among the three GO types (figure 2(C)), this was not statistically significant between s-GO and us-GO (figure 3(C)). Nonetheless, the size distribution was narrower for us-GO, which contained flakes with lateral dimensions below 340 nm, compared to s-GO, which was characterised by flakes with lateral dimensions below 740 nm. This was also reflected in figure 3(C), where the population of larger flakes that were identified as outliers was more pronounced in us-GO. The flake thickness for all three materials was also measured using AFM height scans. Typical cross section of l-GO samples and thickness boxplot distributions are shown in figure 4. The majority of the measured GO flakes in all three types had a thickness between 1 and 4 nm (figure 4(B)), which defined them as single- to few-layer GO materials according to referential nomenclature [5, 6].

Physicochemical characterisation of graphene oxide flakes

In order to understand whether our production method had a significant impact on the physicochemical properties of the resulting three GO materials, we performed a thorough characterisation of each material to evaluate the impact of the

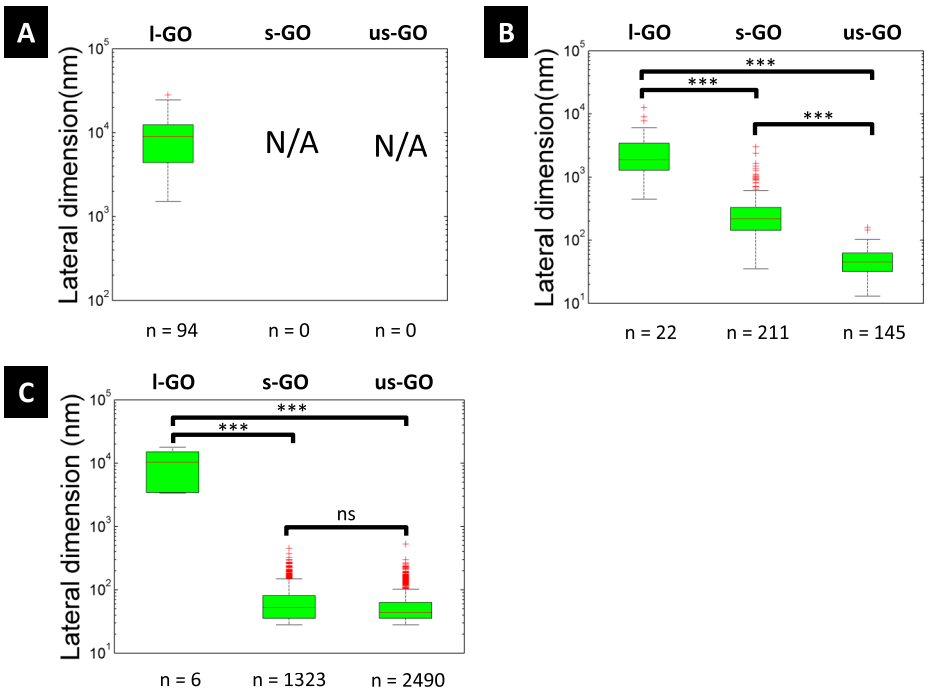

Figure 3. Box plots of the individual sheet lateral dimension for l-GO, s-GO and us-GO using three different imaging techniques: optical microscopy (A); TEM (B); AFM (C). All flakes were counted manually except in the case of the AFM scans for the s-GO and us-GO where a segmentation algorithm was used in ImageJ software. In the case of l-GO, optical microscopy is the only technique which allows the determination of the lateral size distribution by manual counting with a sufficient *n* number. AFM analysis does not show a significant statistical difference between s-GO and us-GO. TEM analysis displays on the other hand a clear significant statistical difference in lateral dimension between the three materials. Statistics were performed using a Wilcoxon rank sum test. ***: $p < 0.001$.

introduction of oxygen functionalities in their optical properties, surface chemistry, colloidal stability and crystal structure.

Optical properties

All GO materials exhibited similar characteristic UV–vis absorbance (figure 5(A)) and fluorescence emission (figure 5(B)) spectra, as revealed by the respective calibration curves that were obtained (figures 5(A) and (B), inset). The absorbance measurements indicated a highly linear correlation between the concentration of GO and the absorbance at 230 nm, which is assigned to $\pi \rightarrow \pi^*$ transitions in sp^2 clusters [24]. A shoulder peak at 300 nm could also be identified, and is associated with $n \rightarrow \pi^*$ transitions of free electron pairs in the oxygen atoms in C=O bonds, present in carbonyl and carboxyl groups [24, 25]. On the other hand, the fluorescence emission from GO was broad and reproducible for all three types, ranging from 400 to 800 nm with an emission peak around 600 nm. The similar calibration curves obtained for all 3 dispersions indicated that the production steps did not affect significantly the optical properties of GO.

Identification of chemical features

All three GO types exhibited comparable colloidal stability in water, according to ζ-potential measurements (figure 6(A)). In addition, the Raman spectra obtained upon the irradiation with a 633 nm laser indicated the appearance of defects in the crystal structure of graphene (figure 6(B)), as indicated by the emergence of a typical D band (~1338 cm^{-1}) as opposed to the G band (~1590 cm^{-1}). The effect of oxidation of graphite in the crystal structure of GO was quantitatively studied by calculating the ratio between the Raman intensities of the D and G bands (I_D/I_G). This ratio did not significantly differ among the three GO materials.

Fourier transform infrared (FTIR) spectra were obtained to confirm the presence and identify more precisely of oxygen functionalities on the surface of GO (figure 6(C)). FTIR spectroscopy revealed a broad band between 3000 cm^{-1} and 3700 cm^{-1}, corresponding to O–H stretching vibrations characteristic of adsorbed water molecules, hydroxyl and carboxyl groups [22, 26, 27]. A minor feature around 2815 cm^{-1} could be attributed to the presence of aliphatic C–H stretching vibrations [28]. In contrast, a sharp peak around 1725 cm^{-1} indicated the presence of carbonyl and carboxyl groups by C=O stretching vibrations [22, 27]. The contribution of the cyclic aromatic networks is shown by the presence of weak peaks in the 1500–1600 cm^{-1} region (figure S1, supporting information) corresponding to in-plane vibrations [26]; however, the potential contribution of the O–H bending mode of residually adsorbed water molecules, which could be identified around 1625 cm^{-1} should not be excluded [29, 30]. A strong absorption band around 1400 cm^{-1} could be assigned to O–H bending vibrations in hydroxyls [29, 30]. Furthermore,

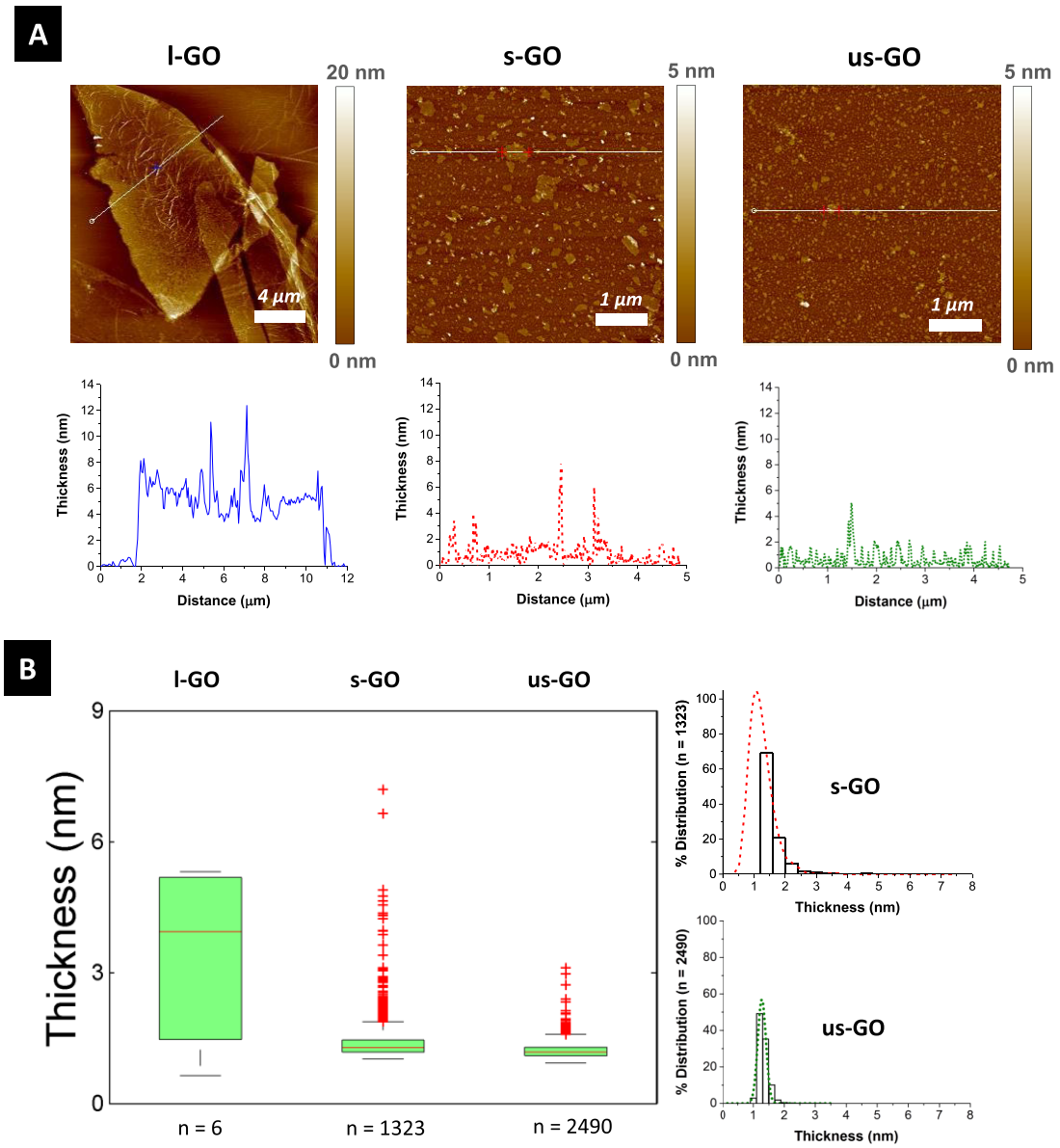

Figure 4. Thickness characterisation of l-GO, s-GO and us-GO: (A) flake cross section and (B) thickness distribution plotted as boxplot and histogram. These distributions were obtained by using a segmentation algorithm on one AFM scan.

the presence of ethers is described by intense absorption bands around 1045 cm^{-1} and 965 cm^{-1}, which correspond to C–O stretching vibrations [22, 31], with epoxides in particular exhibiting C–O bending vibrations around 850 cm^{-1} [31]. All 3 GO materials exhibited similar FTIR spectra, with minor differences observed particularly in the us-GO sample (figure 6(C)). Besides a lower intensity of the band around 1725 cm^{-1}, us-GO also presented a less pronounced band around 1195 cm^{-1}, which could be attributed to C–O stretching in phenols [30].

Quantification of chemical functionalisation and purity

The introduction of oxygen functionalities on the surface of GO was quantified by thermogravimetric analysis (TGA) and x-ray photoelectron spectroscopy (XPS). Two main weight loss steps at temperatures above 100 °C were identified in the TGA curves (figure 6(D)). In our measurements, the contribution of water corresponded to about 10% of the initial weight loss at temperatures below 100 °C. The first weight loss step occurred between 100 °C and 250 °C and is mainly credited to the release of combustion products of the more reactive functionalities such as the carboxyl and epoxy groups [26]. The second weight loss step occurred between 250 °C and 470 °C, which describes the decomposition of more thermally stable groups such as carbonyls and hydroxyls, alongside the pyrolysis of residual carboxyls and ethers [26, 32]. No obvious differences in the functionalisation degree were identified by TGA (figure 6(D)), as a similar first weight loss step of ~27% was obtained for all GO samples (table S2, supporting information). Furthermore, the second step resulted in comparable

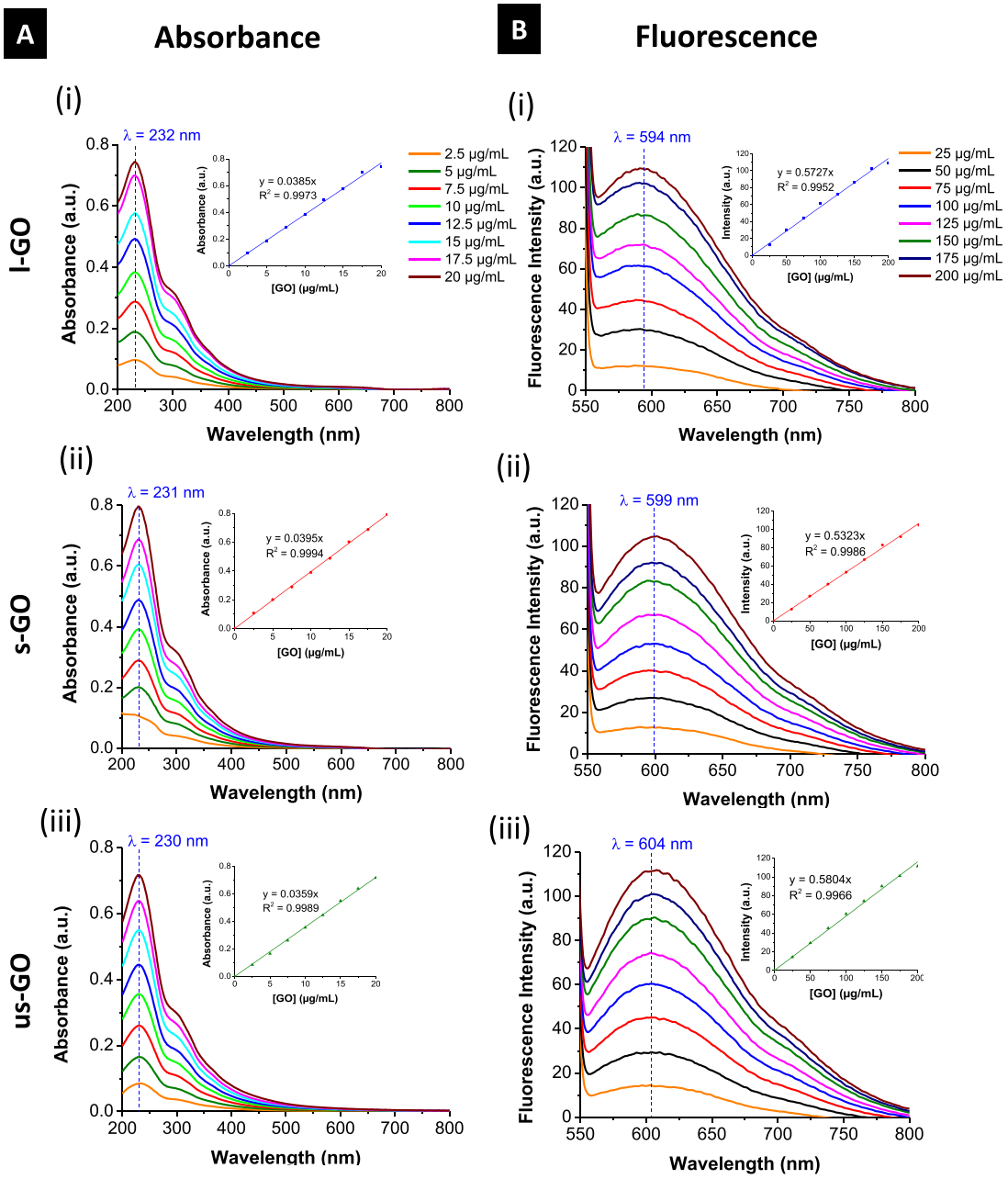

Figure 5. Optical properties of l-GO (i), s-GO (ii) and us-GO (iii). (A) UV–vis spectra of GO at concentrations ranging between 2.5 and 20 μg ml^{-1}, with inset calibration curve at the wavelength of maximum absorbance. (B) Fluorescence emission spectra at the excitation wavelength of 525 nm of GO at concentrations ranging between 25 and 200 μg ml^{-1}, with inset calibration curve at the wavelength of maximum fluorescence intensity.

contributions of oxygen functionalities for l-GO (9.1%), s-GO (11.7%) and us-GO (9.7%), despite minor variations in thermal stability. Further quantification of the functionalisation of GO was achieved by acquiring XPS spectra (figure 7). The survey spectra (figure S2 and table S3, supporting information) demonstrated the high chemical purity of GO by evidencing only minute atomic impurities such as nitrogen and sodium (<0.5%), compared to the typical contributions of the 1s electron of carbon (C1s) and oxygen (O1s) atoms in GO. Moreover, similar C:O ratios were calculated for the three GO types (2.1–2.2) to indicate similar oxidation degree.

Further analysis of the C1s spectra was performed following the deconvolution of the high-resolution C1s spectra to 1 asymmetric Lorentzian function and 4 Gaussian–Lorentzian components, with peaks centred at 284.6, 286.5, 287.8, 288.6, and 290.2 eV (figure 7(A)). These binding energy values were attributed to the formation of: (i) sp^2 and sp^3 hybridisations of carbon (C–C and C=C) in the graphitic backbone; (ii) single bonds between carbon and oxygen (C–O) in hydroxyls and ethers, including phenols and epoxides, respectively; (iii) double bonds between carbon and oxygen (C=O), indicating the presence of carbonyl groups in the form of aldehydes, ketones and quinones; (iv) multiple bonds between carbon and oxygen, resulting in the occurrence of carboxyls, anhydrides and esters, such as lactones (O–C=O) [32–34]. The fifth component corresponds to the satellite peak

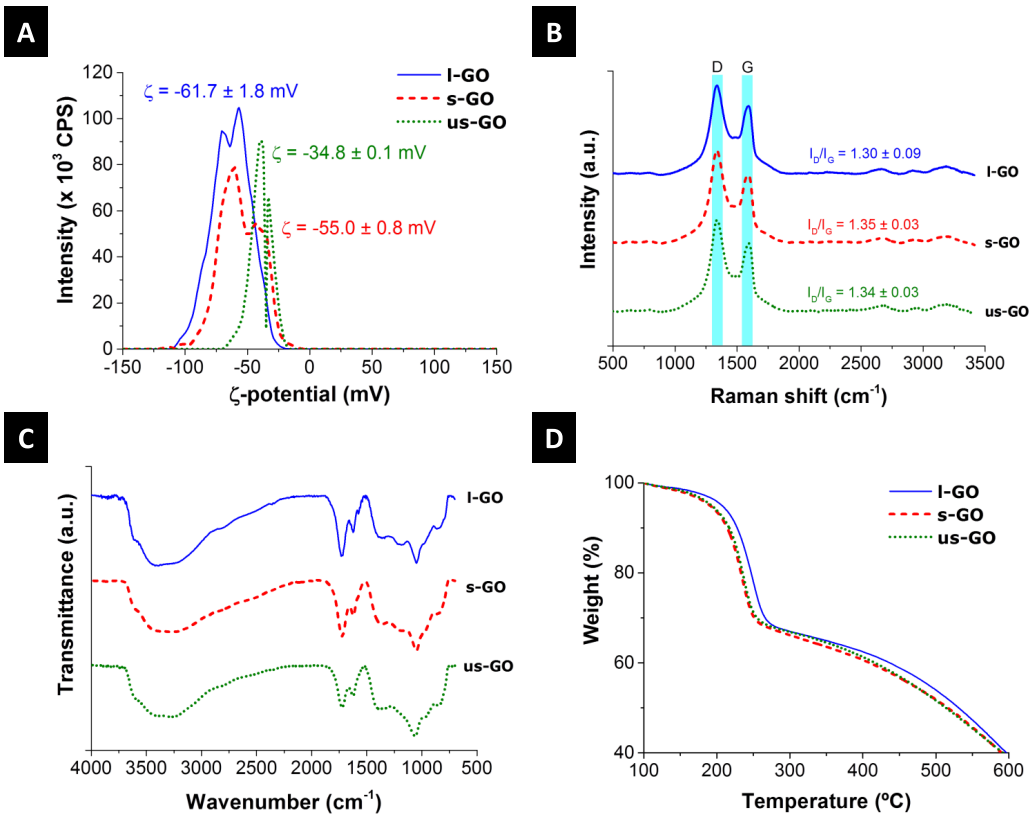

Figure 6. Surface characterisation of GO. (A) Zeta potential measurements of the three materials confirm the presence of negative charges brought by the oxygen functional groups decorating the carbon lattice. (B) Raman spectra of GO with different lateral dimensions with corresponding I_D/I_G ratios. (C) FTIR spectra of GO samples describe the contribution of several surface functionalities. (D) TGA curves highlight the contribution of these functionalities to the thermal decomposition of GO.

π–π^* due to the presence of delocalised π electrons in the graphene lattice [34, 35]. The high-resolution O1s spectra were also deconvoluted to 3 components fitted by Gaussian–Lorentzian functions, peaking at 530.7, 532.2, and 533.9 eV (figure 7(B)). These energies could be attributed to: (i) O=C bonds from the aforementioned carbonyl and carboxyl groups; (ii) O–C bonds from hydroxyls and ethers; (iii) O–C in carboxyls and esters (O=C–O), respectively [35, 36]. The combination of both C1s and O1s spectra validated our fitting assignments, and revealed a high degree of oxidation of all 3 GO materials, with C–O bonds dominating the surface chemistry (tables S4 and S5, supporting information). Although we could observe a slightly lower abundance of C–O bonds in the C1s spectra of us-GO (figure 8(A)), which led to a higher abundance of C–C bonds compared to the other two GO materials, these differences were not statistically significant ($p = 0.1325$). The analysis of the O1s spectra (figure 8(B)), however, indicated a decreased amount of oxygen atoms involved in C–O bonds in us-GO compared to the other GO materials ($p = 0.0417$).

Endotoxin assessment of graphene oxide flakes

The endotoxin content in the synthesised GO flakes was assessed using a cell-based assay designated TET as reported previously [23]. Briefly, primary human monocyte-derived macrophages (HMDMs) were exposed to different concentrations of the 3 GO materials for 24 h (figure 9). Alamar Blue assay showed the lack of cytotoxicity of all GO materials at concentrations up to 75 μg ml^{-1} (figure 9(A)). On the other hand, treatment of HMDMs with 5% DMSO resulted in loss of cell viability to ~45%. No interference from any of the GO samples at the highest concentration used here (75 μg ml^{-1}) was observed in this assay (data not shown).

We therefore chose the non-cytotoxic dose of 50 μg ml^{-1} to measure the endotoxin content of GO by TET. This assay was performed with GO in the presence or absence of the endotoxin inhibitor, polymyxin B sulfate [37], and LPS was included as a positive control. As reported by Mukherjee *et al* [23], if HMDMs exposed to GO or other GBMs produce TNF-α and if the levels of TNF-α are equivalent in the presence or absence of polymyxin B sulfate, then TNF-α production is an intrinsic feature of the GO. When HMDM express less TNF-α upon exposure to GBM in the presence of polymyxin B sulfate then the GBM is contaminated with endotoxin, and if there is no secretion of TNF-α, then there is no endotoxin present [23]. After exposing HMDMs to 50 μg ml^{-1} of GO for 24 h, in the presence or absence of 10 μM polymyxin B sulfate, the supernatants were collected for measurement of secreted TNF-α using ELISA. None of the GO samples triggered significant production of TNF-α in macrophages, irrespective of the presence of polymyxin B (figure 9(B)), indicating that all these tested GOs were,

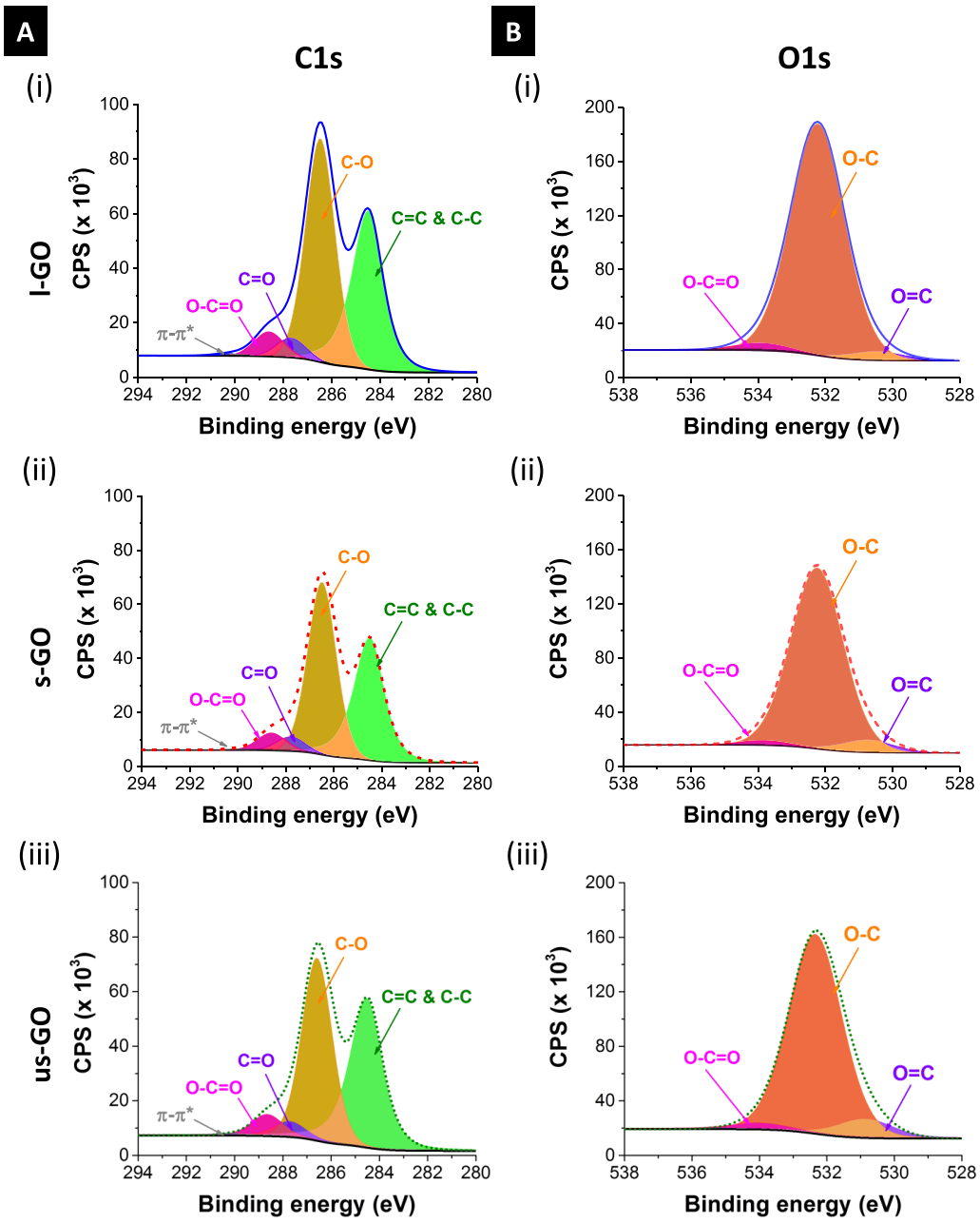

Figure 7. Quantification of surface functionalisation of l-GO (i), s-GO (ii) and us-GO (iii) by XPS. Deconvolution of high resolution C1s (A) and O1s (B) spectra enabled the quantification of functional groups connected to the graphene backbone. Spectra were plotted as the average of 2–3 independent measurements.

in fact, endotoxin-free. After establishing a standard curve using different concentrations of LPS (data not shown), our assay indicated that 50 μg ml^{-1} of GO had a contamination lower than 0.01 EU ml^{-1}.

Discussion

It is widely acknowledged that the size, shape and surface characteristics of nanomaterials greatly determine their biological fate *in vivo*, consequently affecting their potential adverse effects or their bioavailability when used as nanomedicines. More than 30 years ago, Illum *et al.* demonstrated that smaller polystyrene spheres (<1 μm) were more likely to be taken up by the mononuclear phagocyte system, whereas larger particles (>1 μm) were mechanically filtered by the lung capillary beds [38]. Whilst applications such as thin films, composites and electronic devices privilege the use of large, micrometre-sized GBMs [39, 40], recent reviews suggest that chemically modifying the surface of GBMs and reducing their lateral dimensions are two useful strategies to favour their behaviour in physiological milieu and thus improve their biocompatibility [16, 17]. Some reports have also confirmed that GO of greater lateral dimensions has a greater potential of inducing inflammatory responses [41, 42]. Furthermore, the flake thickness has been proven to have an impact on the biodistribution after intravenous administration, as thin GO flakes (~1.2 nm) were found to accumulate less and be more rapidly excreted through the urinary tract than the thick ones (~20 nm) [12], demonstrating an optimal

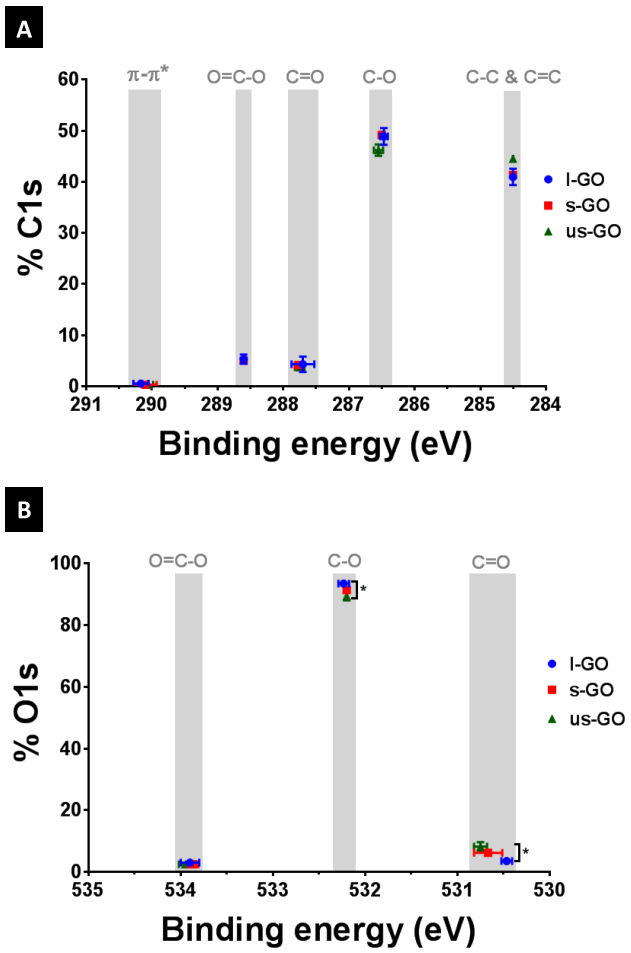

Figure 8. Quantification of surface functionalisation of GO. Quantification of the total contribution of various functional groups deconvoluted in the high resolution C1s (A) and O1s (B) XPS spectra. Data are expressed as mean ± SD (n = 2–3). Statistics were performed for each functional group using a Kruskal–Wallis test with *post hoc* Dunn's multiple comparisons test: (*), $p < 0.05$.

circulation half-life and clearance for thinner materials when considered as nanomedicines.

Controlling lateral dimensions of thin GO flakes, whilst maintaining other physicochemical properties, is therefore crucial to facilitate the design of safer GO-based materials for biomedical applications or when assessing the role of lateral dimensions of GO flakes in their biological impact. However, this has not been well described in the literature when using a top-down exfoliation synthesis approach. For instance, several laboratories have attempted to reach this goal either by oxidising the GO flakes to different extent [43] and/or using different starting graphite materials [44, 45], or by performing sonication followed by several separation techniques. These techniques rely on the physical deposition of GO flakes depending on their lateral dimensions and thickness, which can be naturally obtained by density gradient ultracentrifugation [46, 47] and membrane ultrafiltration [48], or by altering the chemical environment with the addition of acids and organic solvents, which ultimately change the colloidal stability of GO flakes in aqueous dispersions [49, 50].

In the present work, we prepared three different GO materials via a modified version of the Hummers' method under previously described endotoxin-free conditions [22, 23]. Our production process is characterised by the purification of graphite oxide that is synthesised after the conventional Hummers' method [21]. Since this graphite oxide might still contain residual reagents such as manganese salts and the highly reactive dimanganese heptoxide [7], we performed multiple centrifugation rounds to progressively purify the mixture and remove these chemical impurities, alongside other metallic species and fulvic acids (figure 1(A)). This purification step is not only essential to obtain the so called 'GO layer' as previously described [14, 22], but also to guarantee its high chemical purity. Barbolina *et al* previously demonstrated that high concentrations of manganese and sulphur, resulting from the original Hummers' method, could have a highly detrimental impact on bacterial viability [51]. On the other hand, neutralised and purified GO dispersions did not exert any significant effect compared to the deionised water control. The strict and controlled separation of the GO flakes from these toxic impurities was therefore implemented in our process in order to guarantee a highly pure GO product, which can be confidently assessed in terms of its biological effects following its exposure to biological systems.

This purification step was also implemented to remove graphitic impurities from the final l-GO product (figure 1(B)), due to their greater sedimentation rate compared to l-GO flakes.

Then, we employed ultra-sonication followed by a high-speed centrifugation step to yield purified s-GO and us-GO materials (figure 1(B)). The process to obtain either s-GO or us-GO differed only in the duration of the sonication step (5 min and 4 h, respectively). During sonication, GO flakes were shown to undergo physical breakdown due to the formation and propagation of cracks that are catalysed by the presence of sp^3 defects in the basal plane of the graphene lattice [52]. Gonçalves *et al* also postulated that ultrasound waves induce cavitations that could result in local increase of temperature, promoting the release of both adsorbed water molecules and oxygen functionalities. Thus, we attempted to minimise a potential thermal reduction of GO by performing ultra-sonication in a sonication bath kept under a set temperature ($T < 40\,^{\circ}C$), instead of directly sonicating the dispersion using a probe that could contaminate our final s-GO and us-GO materials with by-products coming from the probe [53].

Despite precautions, thermal reduction of GO can still occur at temperatures as low as 50 °C, as a result of the reaction of carboxyl groups with water, releasing CO_2 [26]. Hence, one could expect that longer sonication times would yield smaller but slightly more reduced GO flakes. Moreover, longer sonication times could increase the density of defects across the graphene lattice. We therefore tested the impact of sonication on various physicochemical features including the surface chemistry and crystal structure of the resulting materials, namely s-GO and us-GO. All GO materials exhibited similar optical properties (figure 5), which could be associated to similar abundance of C=O bonds from carbonyl and carboxyl groups, as the oxygen atoms provide free electron pairs to perform $n \rightarrow \pi^*$ transitions, linked to the absorbance at 300 nm (figure 5(A)), and confer photoluminescence to GO (figure 5(B)). The photoluminescence of GO could be studied using an excitation wavelength around 525 nm, which could be linked to $\pi \rightarrow \pi^*$ transitions in the sp^2 hybridised aromatic network of graphene [25]. However, we have also identified multiple excitation wavelengths that replicate the broad fluorescence emission band peaking around 600 nm [54]. They have been associated with the variety of oxygen functionalities in GO, which provide free electrons that contribute for the electronic transitions required for fluorescence emission [25, 55].

Given the improved linear relationship between fluorescence intensity and concentration of GO at 525 nm, we used this wavelength, alongside the absorbance peak at 230 nm, to quantitatively characterise the optical properties of our materials (figure 5, insets). The similar calibration curves obtained for the three different types at $\lambda_{exc} = 525$ nm indicate that the production steps (including sonication) did not affect significantly the optical properties of GO. Understanding the photochemical properties of GO not only allows the quantification of material in colloidal dispersion but also enables their exploitation in biomedicine. One recently reported example is the use of time-lapse confocal fluorescence microscopy to visualise the behaviour of cells in real time after exposure to the material [54].

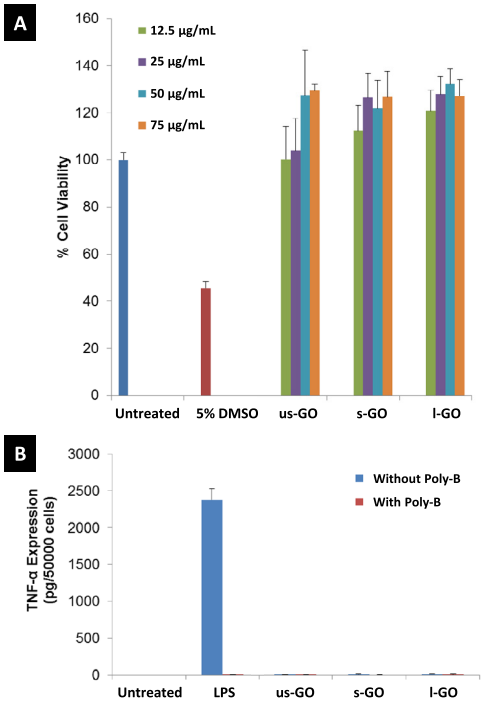

Figure 9. Endotoxin assessment of GO samples. (A) Alamar blue assay indicated the lack of cytotoxicity of any of the 3 GO materials towards HMDMs exposed at relevant concentrations for the TET. (B) TET demonstrated that all the tested GO samples were endotoxin-free as they did not trigger significant TNF-α production either in the presence or absence of polymyxin B (Poly-B). As a positive control, stimulation with LPS (0.1 μg ml^{-1}) resulted in secretion of TNF-α, which was blocked by Poly-B. Data are expressed as mean values $\pm$ S.D. At least 4 replicates were used for each exposure condition.

The introduction of oxygen functionalities across the graphene lattice was confirmed qualitatively through several techniques including ζ-potential, Raman and FTIR spectroscopy measurements, which all indicated the chemical transformation of the starting graphite. All three GO materials evidenced similar colloidal stability in ultrapure water (figure 6(A)). The stability of GO in polar solvents is determined by the presence of oxygen functionalities, particularly carboxyl and hydroxyl groups, which can confer a negative charge to the surface of GO flakes and mediate electrostatic repulsion forces between them, thus preventing aggregation of the materials in water [25, 56].

It is thought that these oxygen functionalities are present in defected sp^3 sites within the sp^2 lattice of graphene, as a result of the oxidation of graphite. Consistent with previous studies, all three GO materials had a negligible 2D peak (~2660 cm^{-1}) compared to what was previously observed for the start-

ing graphite source [22], giving rise to the first order D band (~1338 cm^{-1}). Broad D and G bands were rather observed in the Raman spectra of the three GO samples (figure 6(B)), describing the introduction of defects in the graphene lattice [22, 57]. The I_D/I_G ratio did not significantly differ among the three GO materials, implying that the sonication time did not further increase the amount of defects in the graphene lattice with the introduction of additional oxygen functionalities, which would otherwise increase the I_D/I_G ratio.

All three GO types exhibited similar FTIR spectra, despite small differences between us-GO and the other 2 materials (figure 6(C)). In particular, the lower intensities of the bands around 1725 cm^{-1} and 1195 cm^{-1} suggest that us-GO might have a slightly lower abundance of carbonyls and phenols, respectively, which could explain the minor differences observed by ζ-potential measurements (figure 6(A)). However, these minor differences need to be quantitatively analysed to better understand whether and how the chemical micro-environment has changed with sonication to yield us-GO from l-GO, compared to s-GO.

In order to confirm that the surface chemistry was not significantly modified after sonication, the introduction of oxygen functionalities across the graphene lattice was quantified by TGA and XPS. The functionalisation degree obtained by TGA was similar for all three GO materials, which exhibited similar thermal stability (figure 6(D) and table S2, supporting information). The first weight loss step (100 °C–250 °C) could be related to the greater content of carboxyl and epoxy groups [26, 35], in agreement with the obtained FTIR spectra, where C–O and C=O bonds were expressed to a greater extent (figure 6(C)). Epoxides are under strain due to the location of the oxygen atom out of the basal plane, and thus readily decomposed at high temperatures, generating hydroxyl groups [26, 27]. As a result, this reaction removes some carbon atoms from the graphene lattice, creating localised sp^3 defect states [27]. However, thermal decomposition is a dynamic process, where the more reactive functionalities can be converted to others with lower thermodynamic energy. In this case, the generation of more stable functionalities such as hydroxyls should compensate the loss of epoxides and other ethers [26]. As a result, a second weight loss step could still be identified (250 °C–470 °C) and could be attributed to residual hydroxyls, together with other more stable functionalities such as carbonyls and quinones [35].

XPS survey spectra revealed high chemical purity of all three GO materials (>99.5%), with minor contamination from nitrogen and sodium (figure S2 and table S3, supporting information). These impurities could be due to the reagents used in the Hummers' method [21]. Together with similar C:O ratios (table S3, supporting information), the deconvolution of the high-resolution C1s and O1s spectra (figure 7) showed that the three GO materials had similar surface chemistry, dominated by the formation of C–O bonds characteristic of ethers and hydroxyls. The quantification of the deconvoluted components resulted in a slight lower relative abundance of oxygen atoms involved in C–O bonds in us-GO compared to l-GO (figure 8(B)). This was accompanied by a slightly lower abundance of carbon atoms involved in C–O bonds (figure 8(A)); however it was not statistically significant ($p = 0.1325$). Similarly, the lower abundance of oxygen atoms involved in C=O bonds in l-GO was not observed in the C1s spectra. Taken together, the surface chemistry of all 3 GO materials did not change considerably, despite minor variations in the abundance of C–O bonds.

Assessment of the morphology of graphene oxide flakes

The sonication step employed in the present work was shown to effectively decrease the lateral dimensions of GO flakes (figure 2). The lateral dimensions of l-GO flakes could be easily assessed using optical microscopy due to their micrometric scale (figure 2(A)), whereas the analysis of the lateral dimensions of s-GO and us-GO flakes required both TEM (figure 2(B)) and AFM (figure 2(C)). The lateral dimensions of GO flakes are characterised by a log-normal distribution that not only spans multiple orders of magnitude, but also has a pronounced skewness [58]. Instead of conventionally plotting this distribution as a histogram, the boxplot representation can remove the interpretation bias caused by a small number of larger flakes, which can be assumed as outliers.

AFM enabled the observation of a greater number of smaller GO flakes, which adhered better to the mica substrates coated with positively charged poly-*L*-lysine. Despite a clear size difference visually observable on AFM scans, the boxplots did however not reveal a dramatic change in terms of lateral dimensions between s-GO and us-GO (figure 3(C)). The boxplots suggest that the sonication time affected preferentially the remaining larger GO flakes in s-GO and induced their break down into smaller pieces during the production of us-GO, thus narrowing the overall size distribution of us-GO in comparison to s-GO. However, we cannot exclude other possible explanations for the lack of statistical significance, such as the limitations of the segmentation algorithm used to discriminate the GO flakes on AFM scans, which may include pixel artefacts or unsatisfying segmentation of nearby flakes which led to the fusion of several sheets all together.

Despite the technical difficulty of imaging s-GO and us-GO flakes with a high enough contrast, TEM appears as the best compromise among the three microscopic techniques when comparing the lateral dimensions of all three materials (figure 3(B)). Using TEM, we were able to detect more flakes within a wide range of sizes. The magnification must however be carefully set up, as higher magnifications tend to bias the results by excluding the largest flakes within the

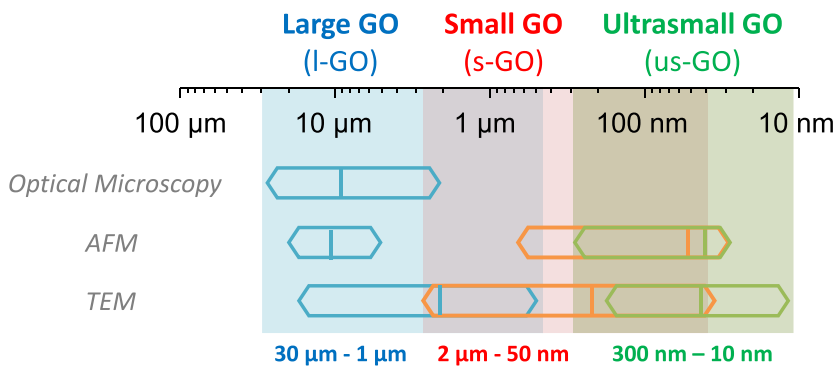

Figure 10. Comparison of lateral dimensions of GO flakes measured using multiple imaging techniques. The combination of these techniques provided a range of flake sizes which increases the confidence of our analysis.

population. The detection by TEM of submicron-sized flakes in l-GO skewed the average flake size of these materials to lower values compared to values obtained with optical microscopy or AFM (table S1).

The three materials displayed very distinct lateral dimensions, whose distributions span across less than an order of magnitude for each one of them (figure 10). Therefore, in order to cover appropriately the range of expected flake size for each sample, an adequate selection of imaging techniques (e.g. optical microscopy, AFM or TEM) must be made. Because it covered the widest range of flakes in our study (figure 10), we conclude that electron microscopy (i.e. TEM or SEM) should be the technique of choice to assess the structural morphology of GBMs. However, the number of detected flakes must be high enough to provide a powerful statistical comparison of lateral dimensions. Optical microscopy appeared as the most convenient technique to observe large flakes such as in l-GO but lacked the resolution to accurately assess the size of small flakes typically found in s-GO and us-GO due to the Abbe's law diffraction limit. Hence, it can be readily used for the quality control of the impact of sonication on visible micrometre-sized flakes, yielding invisible nanometre-sized flakes under the optical microscope (figure 2(A)). Although AFM had a more limited detection of larger GO flakes and is characterised by a low throughput, it also provides invaluable information on the thickness of GBMs (figure 4). Here, all three GO materials were made of a majority of flakes with thickness between 1 and 4 nm, corresponding to single- to few-layer flakes [5, 6]. Individual GO sheets have indeed been reported to have a thickness of about 1 nm, which is slightly thicker than pristine graphene due to the presence of oxygen groups and adsorbed water onto the carbon lattice [59].

Considering the different advantages and limitations of each microscopic technique, we show that when they are used together they can complement each other, ultimately providing more information about the dimensions of GO materials without significant bias. Combining all the microscopic techniques used in the present study (figure 10), we found that l-GO flakes had lateral dimensions varying between 1 and 30 μm, s-GO flakes ranged between 50 nm and 2 μm and us-GO flakes were smaller than 500 nm.

Impact of sonication on the physicochemical properties of graphene oxide

As mentioned previously, we estimated that the bath sonication step employed in the production of s-GO and us-GO (5 min and 4 h, respectively) may have induced changes in the surface chemistry, potentially reducing the final GO materials. We attempted to minimise these potential changes by carefully monitoring the temperature of the sonication bath and renewing it with ice-cold water frequently. Whilst the three GO materials produced here yielded flakes with lateral dimensions inversely proportional to sonication time, the remaining physicochemical properties did not change considerably. However, it must be noted that no further change in lateral dimensions was observed beyond 4 h of sonication, i.e. no further size reduction (data not shown). These findings are in agreement with other studies on the impact of bath sonication on the flake size of GO [60].

We carefully analysed the surface chemistry of the produced GO materials using complementary techniques. Despite the similar functionalisation degree evidenced by TGA (figure 6(D)), ζ-potential measurements (figure 6(A)) and FTIR spectroscopy (figure 6(C)) suggested minor changes to the chemistry of us-GO flakes, with potentially lower abundance of carboxyls and hydroxyls or ethers, which could reduce their colloidal stability. Using XPS, we quantitatively assessed those changes, which consisted in a minor decrease of C–O bonds evidenced in high-resolution O1s spectra (figure 8). Taken together, these results indicate that the overall surface chemistry of GO flakes was not significantly affected by sonication. We hypothesise that the observed changes are due to the breakage of ethers, including epoxides, during the sonication process. Epoxides are a particular type of sp^3 defects present in GO, that are attributed with greater strain, compared to other oxygen functionalities, and hence are more prone to break under sonication [52,

61]. As they should populate the basal plane of GO, they offer several hot spots to break down into smaller flakes. Various studies have predicted that consecutive epoxy groups aligned on the basal plane could promote the formation of cracks due to the increased strain exerted on the graphene lattice [62, 63]. This would lead to the separation of C–O–C to form C=O and C–H [63], which would lead to a more dramatically decreased abundance of C–O bonds in the O1s spectra, as observed here (figure 8(B)).

Therefore, our sonication protocol promoted specifically the breakage of larger GO flakes through the already oxidised sp^3 defects, as suggested by the AFM images (figure 2(C)). This phenomenon is also supported by the reduced polydispersity observed between s-GO and us-GO (figure 3(C)). The mild conditions used to sonicate GO could specifically reduce the lateral dimensions to produce different flake sizes whilst conserving all other examined properties. This conclusion was also supported by Raman spectroscopy (figure 6(C)), which suggested that the sonication step did not affect the crystal structure of GO. Additional techniques such as electron diffraction could provide more detailed information on the disruption of the crystal structure of GO due to the chemical exfoliation employed here. This physical breakage seems to have been accompanied by the hydration of oxygen functional groups at the newly formed edges, which is supported by the maintenance of the relative amount of carboxylic acids in GO, irrespective of lateral dimensions, as shown by XPS. Rearrangement reactions between these newly formed edges in the smaller GO flakes and the adsorbed water molecules could have resulted in the formation of carboxylic acids [26].

Overall, our method has proven to provide an aqueous dispersion of highly dispersible GO flakes, which are non-pyrogenic and chemically stable in water at room temperature for more than 6 months [22]. The maintenance of the surface chemistry is of utmost importance, especially considering that the degree of oxidation also plays a role in the biocompatibility of GO [64]. Reduced GO may agglomerate to a greater extent in physiological *milieu*, which can affect the rate and extent to which they are cleared from the body [64]. Therefore, maintaining the surface chemistry within stringent standards enables the assessment of the biological impact of the structural properties of GBMs such as lateral dimensions and thickness.

Finally, the importance of using non-pyrogenic materials for the analysis of biological interactions of 2D materials should not be ignored. Regulatory authorities have fixed a limit for endotoxin contamination in order for any material to be used in the clinic [65]. Using a cell-based assay (figure 9), we observed that all three GO materials produced in the present work complied with the endotoxin limit of 0.5 EU ml^{-1}, established for medical devices that contact the cardiovascular and lymphatic systems [65]. Therefore, our materials met the non-pyrogenic criteria required for their biomedical application and hazard assessment [23, 65]. This is a non-trivial issue as endotoxin-contaminated nanomaterials can show inflammatory or toxic effects which may mask or confound the real biological effects (or lack thereof) [66].

Towards standardisation of graphene oxide materials for biological applications

The adoption of GBMs in commercial products requires their scalable and reproducible production [4]. Currently there are numerous strategies to produce GBMs with a variety of physicochemical properties, which raises the call for standardisation. Standardisation has been applied to the classification of GBMs [5, 6], which resulted in the recent terminology standard ISO/TS 80004-13 [67]. Nevertheless, this initial effort needs to be followed by the establishment of suitable techniques to probe the physicochemical properties of GBMs, so they can be correctly classified [68]. This is even more paramount in biomedicine [20], where quality control requirements are more stringent.

The characterisation pipeline used here to study the physicochemical properties of GO flakes allowed the meticulous assessment of their lateral size, thickness, surface chemistry, colloidal stability and endotoxin contamination. A similar strategy has been recently applied to the observation of graphene oxide sheets using similar microscopic techniques to our study [69]. Our proposed systematic approach is expanded to cover the surface chemistry of GO, which will affect many of the desired properties of GBMs in industry and will determine the definition of Health and Safety standards [68].

In the present work, the combination of multiple techniques can help to circumvent experimental bias and/or uncertainties when assessing a given property of the considered material. The proposed systematic approach for characterisation should address the concerns that have been recently raised within the scientific community regarding the need for a comprehensive understanding and the standardisation of nanomaterials through curated data [68, 70].

Conclusion

The present study described the production of three types of non-pyrogenic, highly pure (>99%), single-to-few-layer GO sheets which were found to differ only by their lateral dimensions, without considerably changing neither the surface chemistry nor the thickness, after careful physicochemical characterisation. The mild conditions used during sonication ensured the maintenance of similar surface chemistry properties. We highlighted the need for using complementary techniques to characterise the physicochemical properties and to reduce potential experimental errors and/or inaccuracies. Combining three microscopic techniques, we found that the produced l-GO flakes

had lateral dimensions varying between 1 and 30 μm, s-GO flakes ranged between 50 nm and 2 μm and us-GO flakes were smaller than 500 nm. Therefore, we showed that non-pyrogenic GO flakes can be produced with controlled lateral dimensions. Future studies should investigate how lateral dimension of GO sheets may affect their biological impact and their cellular, tissue and whole body interactions.

Acknowledgments

This work was supported by the European Commission through the GRAPHENE Flagship Project (grant agreements no. 604391 and 696656). AFR would like to acknowledge a studentship from the EPSRC Centre for Doctoral Training in the Science and Applications of Graphene and Related Nanomaterials (GrapheneNOWNANO CDT; EP/L01548X/1). LN is indebted to EPSRC for his studentship in the framework of the EPSRC-funded North West Nanoscience Doctoral Training Centre (NOWNANO DTC; EP/G03737X/1). We would like to acknowledge various teams from the FBMH Platform Sciences, Enabling Technologies and Infrastructure at The University of Manchester: Dr Michael Sherratt and Dr Nigel Hodson (BioAFM facility) regarding the AFM instrumentation and image processing; the staff in the EM Facility and the Wellcome Trust for equipment grant support to the EM Facility; The Bioimaging Facility microscopes used in this study were purchased with grants from the BBSRC, Wellcome Trust and the University of Manchester Strategic Fund. The x-ray photoelectron spectra were obtained at the National EPSRC XPS Users' Service (NEXUS) at Newcastle University. We finally would like to acknowledge the advice of Prof Nicola Tirelli (School of Health Sciences, The University of Manchester, UK; IIT Genova, Italy) regarding the FTIR measurements.

ORCID iDs

Artur Filipe Rodrigues https://orcid.org/0000-0002-4078-3455
Bengt Fadeel https://orcid.org/0000-0001-5559-8482
Cyrill Bussy https://orcid.org/0000-0001-8870-443X
Kostas Kostarelos https://orcid.org/0000-0002-2224-6672

References

[1] Novoselov K S, Geim A K, Morozov S V, Jiang D, Zhang Y, Dubonos S V, Grigorieva I V and Firsov A A 2004 Electric field effect in atomically thin carbon films *Science* **306** 666–9
[2] Novoselov K S, Fal'ko V I, Colombo L, Gellert P R, Schwab M G and Kim K 2012 A roadmap for graphene *Nature* **490** 192–200
[3] Geim A K 2010 Random walk to graphene *Nobel Lecture* (www.nobelprize.org/nobel_prizes/physics/laureates/2010/geim-lecture.html) (Accessed: 5 May 2018)
[4] Zurutuza A and Marinelli C 2014 Challenges and opportunities in graphene commercialization *Nat. Nanotechnol.* **9** 730–4
[5] Bianco A *et al* 2013 All in the graphene family—a recommended nomenclature for two-dimensional carbon materials *Carbon* **65** 1–6
[6] Wick P *et al* 2014 Classification framework for graphene-based materials *Angew. Chem., Int. Ed.* **53** 7714–8
[7] Dreyer D R, Park S, Bielawski C W and Ruoff R S 2010 The chemistry of graphene oxide *Chem. Soc. Rev.* **39** 228–40
[8] Kostarelos K and Novoselov K S 2014 Graphene devices for life *Nat. Nanotechnol.* **9** 744–5
[9] Bitounis D, Ali-Boucetta H, Hong B H, Min D H and Kostarelos K 2013 Prospects and challenges of graphene in biomedical applications *Adv. Mater.* **25** 2258–68
[10] Georgakilas V, Otyepka M, Bourlinos A B, Chandra V, Kim N, Kemp K C, Hobza P, Zboril R and Kim K S 2012 Functionalization of graphene: covalent and non-covalent approaches, derivatives and applications *Chem. Rev.* **112** 6156–214
[11] Jasim D A, Menard-Moyon C, Begin D, Bianco A and Kostarelos K 2015 Tissue distribution and urinary excretion of intravenously administered chemically functionalized graphene oxide sheets *Chem. Sci.* **6** 3952–64
[12] Jasim D A, Boutin H, Fairclough M, Ménard-Moyon C, Prenant C, Bianco A and Kostarelos K 2016 Thickness of functionalized graphene oxide sheets plays critical role in tissue accumulation and urinary excretion: a pilot PET/CT study *Appl. Mater. Today* **4** 24–30
[13] Jasim D A *et al* 2016 The effects of extensive glomerular filtration of thin graphene oxide sheets on kidney physiology *ACS Nano* **10** 10753–67
[14] Ali-Boucetta H, Bitounis D, Raveendran-Nair R, Servant A, Van den Bossche J and Kostarelos K 2013 Purified graphene oxide dispersions lack *in vitro* cytotoxicity and *in vivo* pathogenicity *Adv. Healthcare Mater.* **2** 433–41
[15] Yang K, Feng L, Shi X and Liu Z 2013 Nano-graphene in biomedicine: theranostic applications *Chem. Soc. Rev.* **42** 530–47
[16] Bussy C, Ali-Boucetta H and Kostarelos K 2013 Safety considerations for graphene: lessons learnt from carbon nanotubes *Acc. Chem. Res.* **46** 692–701
[17] Bussy C, Jasim D A, Lozano N, Terry D and Kostarelos K 2015 The current graphene safety landscape—a literature mining exercise *Nanoscale* **7** 6432–5
[18] Bianco A 2013 Graphene: safe or toxic? The two faces of the medal *Angew. Chem., Int. Ed.* **52** 4986–97
[19] Godwin H *et al* 2015 Nanomaterial categorization for assessing risk potential to facilitate regulatory decision-making *ACS Nano* **9** 3409–17
[20] Kostarelos K 2016 Translating graphene and 2D materials into medicine *Nat. Rev. Mater.* **1** 16084
[21] Hummers W S and Offeman R E 1958 Preparation of graphitic oxide *J. Am. Chem. Soc.* **80** 1339
[22] Jasim D A, Lozano N and Kostarelos K 2016 Synthesis of few-layered, high-purity graphene oxide sheets from different graphite sources for biology *2D Mater.* **3** 14006
[23] Mukherjee S, Lozano N, Kucki M, del Rio-Castillo A, Newman L, Vázquez E, Kostarelos K, Wick P and Fadeel B 2016 Detection of endotoxin contamination of graphene based materials using the TNF-α expression test and guidelines for endotoxin-free graphene oxide production *PLoS One* **11** e0166816
[24] Kumar P V, Bardhan N M, Tongay S, Wu J, Belcher A M and Grossman J C 2014 Scalable enhancement of graphene oxide properties by thermally driven phase transformation *Nat. Chem.* **6** 151–8
[25] Zhang X F, Shao X and Liu S 2012 Dual fluorescence of graphene oxide: a time-resolved study *J. Phys. Chem.* A **116** 7308–13
[26] Eigler S, Dotzer C, Hirsch A, Enzelberger M and Müller P 2012 Formation and decomposition of CO_2 intercalated graphene oxide *Chem. Mater.* **24** 1276–82
[27] Acik M, Mattevi C, Gong C, Lee G, Cho K, Chhowalla M and Chabal Y J 2010 The role of intercalated water in multilayered graphene oxide *ACS Nano* **4** 5861–8

[28] Figueiredo J L, Pereira M F R, Freitas M M A and Órfão J J M 1999 Modification of the surface chemistry of activated carbons *Carbon* **37** 1379–89
[29] Xu Y, Bai H, Lu G, Li C and Shi G 2008 Flexible graphene films via the filtration of water-soluble noncovalent functionalized graphene sheets *J. Am. Chem. Soc.* **130** 5856–7
[30] Szabó T, Berkesi O, Forgó P, Josepovits K, Sanakis Y, Petridis D and Dékány I 2006 Evolution of surface functional groups in a series of progressively oxidized graphite oxides *Chem. Mater.* **18** 2740–9
[31] Acik M, Lee G, Mattevi C, Chhowalla M, Cho K and Chabal Y J 2010 Unusual infrared-absorption mechanism in thermally reduced graphene oxide *Nat. Mater.* **9** 840–5
[32] Ganguly A, Sharma S, Papakonstantinou P and Hamilton J 2011 Probing the thermal deoxygenation of graphene oxide using high-resolution *in situ* x-ray-based spectroscopies *J. Phys. Chem.* C **115** 17009–19
[33] Yang D *et al* 2009 Chemical analysis of graphene oxide films after heat and chemical treatments by x-ray photoelectron and Micro-Raman spectroscopy *Carbon* **47** 145–52
[34] Gao W, Alemany L B, Ci L and Ajayan P M 2009 New insights into the structure and reduction of graphite oxide *Nat. Chem.* **1** 403–8
[35] Araújo M P, Soares O S G P, Fernandes A J S, Pereira M F R and Freire C 2017 Tuning the surface chemistry of graphene flakes: new strategies for selective oxidation *RSC Adv.* **7** 14290–301
[36] Rozada R, Paredes J I, Villar-Rodil S, Martínez-Alonso A and Tascón J M D 2013 Towards full repair of defects in reduced graphene oxide films by two-step graphitization *Nano Res.* **6** 216–33
[37] Cavaillon J-M and Haeffner-Cavaillon N 1986 Polymyxin-B inhibition of LPS-induced interleukin-1 secretion by human monocytes is dependent upon the LPS origin *Mol. Immunol.* **23** 965–9
[38] Ilium L, Davis S S, Wilson C G, Thomas N W, Frier M and Hardy J G 1982 Blood clearance and organ deposition of intravenously administered colloidal particles. The effects of particle size, nature and shape *Int. J. Pharm.* **12** 135–46
[39] Zhao J, Pei S, Ren W, Gao L and Cheng H M 2010 Efficient preparation of large-area graphene oxide sheets for transparent conductive films *ACS Nano* **4** 5245–52
[40] Vallés C, Abdelkader A M, Young R J and Kinloch I A 2014 Few layer graphene–polypropylene nanocomposites: the role of flake diameter *Faraday Discuss.* **173** 379–90
[41] Yue H, Wei W, Yue Z, Wang B, Luo N, Gao Y, Ma D, Ma G and Su Z 2012 The role of the lateral dimension of graphene oxide in the regulation of cellular responses *Biomaterials* **33** 4013–21
[42] Ma J, Liu R, Wang X, Liu Q, Chen Y, Valle R P, Zuo Y Y, Xia T and Liu S 2015 Crucial role of lateral size for graphene oxide in activating macrophages and stimulating pro-inflammatory responses in cells and animals *ACS Nano* **9** 10498–515
[43] Zhang L, Liang J J, Huang Y, Ma Y F, Wang Y and Chen Y S 2009 Size-controlled synthesis of graphene oxide sheets on a large scale using chemical exfoliation *Carbon* **47** 3365–8
[44] Chen J, Chi F, Huang L, Zhang M, Yao B, Li Y, Li C and Shi G 2016 Synthesis of graphene oxide sheets with controlled sizes from sieved graphite flakes *Carbon* **110** 34–40
[45] Botas C, Pérez-Mas A M, Álvarez P, Santamaría R, Granda M, Blanco C and Menéndez R 2013 Optimization of the size and yield of graphene oxide sheets in the exfoliation step *Carbon* **63** 576–8
[46] Sun X, Liu Z, Welsher K, Robinson J T, Goodwin A, Zaric S and Dai H 2008 Nano-graphene oxide for cellular imaging and drug delivery *Nano Res.* **1** 203–12
[47] Sun X, Luo D, Liu J and Evans D G 2010 Monodisperse chemically modified graphene obtained by density gradient ultracentrifugal rate separation *ACS Nano* **4** 3381–9
[48] Chen J, Li Y, Huang L, Jia N, Li C and Shi G 2015 Size fractionation of graphene oxide sheets via filtration through track-etched membranes *Adv. Mater.* **27** 3654–60
[49] Wang X, Bai H and Shi G 2011 Size fractionation of graphene oxide sheets by pH-assisted selective sedimentation *J. Am. Chem. Soc.* **133** 6338–42
[50] Zhang W, Zou X, Li H, Hou J, Zhao J, Lan J, Fenga B and Liu S 2015 Size fractionation of graphene oxide sheets by the polar solvent-selective natural deposition method *RSC Adv.* **5** 146–52
[51] Barbolina I, Woods C R, Lozano N, Kostarelos K, Novoselov K S and Roberts I S 2016 Purity of graphene oxide determines its antibacterial activity *2D Mater.* **3** 25025
[52] Gonçalves G, Vila M, Bdikin I, de Andrés A, Emami N, Ferreira R A S, Carlos L D, Grácio J and Marques P A A P 2014 Breakdown into nanoscale of graphene oxide: confined hot spot atomic reduction and fragmentation *Sci. Rep.* **4** 6735
[53] Taurozzi J S, Hackley V A and Wiesner M R 2011 Ultrasonic dispersion of nanoparticles for environmental, health and safety assessment—issues and recommendations *Nanotoxicology* **5** 711–29
[54] Vranic S, Rodrigues A F, Buggio M, Newman L, White M R H, Spiller D G, Bussy C and Kostarelos K 2018 Live imaging of label-free graphene oxide reveals critical factors causing oxidative stress-mediated cellular responses *ACS Nano* **12** 1373–89
[55] Shang J, Ma L, Li J, Ai W, Yu T and Gurzadyan G G 2012 The origin of fluorescence from graphene oxide *Sci. Rep.* **2** 792
[56] Shih C-J, Lin S, Sharma R, Strano M S and Blankschtein D 2012 Understanding the pH-dependent behavior of graphene oxide aqueous solutions: a comparative experimental and molecular dynamics simulation study *Langmuir* **28** 235–41
[57] Ferrari A C and Basko D M 2013 Raman spectroscopy as a versatile tool for studying the properties of graphene *Nat. Nanotechnol.* **8** 235–46
[58] Perrozzi F, Prezioso S and Ottaviano L 2015 Graphene oxide: from fundamentals to applications *J. Phys.: Condens. Matter* **27** 13002
[59] Geim A K and Novoselov K S 2007 The rise of graphene *Nat. Mater.* **6** 183–91
[60] Coleman B R, Knight T, Gies V, Jakubek Z J and Zou S 2017 Manipulation and quantification of graphene oxide flake size: photoluminescence and cytotoxicity *ACS Appl. Mater. Interfaces* **9** 28911–21
[61] Pan S and Aksay I A 2011 Factors controlling the size of graphene oxide sheets produced via the graphite oxide route *ACS Nano* **5** 4073–83
[62] Li J L, Kudin K N, McAllister M J, Prud'homme R K, Aksay I A and Car R 2006 Oxygen-driven unzipping of graphitic materials *Phys. Rev. Lett.* **96** 176101
[63] Sun T and Fabris S 2012 Mechanisms for oxidative unzipping and cutting of graphene *Nano Lett.* **12** 17–21
[64] Sydlik S A, Jhunjhunwala S, Webber M J, Anderson D G and Langer R 2015 *In vivo* compatibility of graphene oxide with differing oxidation states *ACS Nano* **9** 3866–74
[65] Food and Drug Administration 2012 *Guidance for Industry—Pyrogen and Endotoxins Testing: Questions and Answers* (www.fda.gov/downloads/drugs/guidancecomplianceregulatoryinformation/guidances/ucm310098.pdf) (Accessed: 21 October 2016)
[66] Li Y, Fujita M and Boraschi D 2017 Endotoxin contamination in nanomaterials leads to the misinterpretation of immunosafety results *Front. Immunol.* **8** 472
[67] Pollard A J and Clifford C A 2017 Terminology: the first step towards international standardisation of graphene and related 2D materials *J. Mater. Sci.* **52** 13685–8
[68] Pollard A J 2016 Metrology for graphene and 2D materials *Meas. Sci. Technol.* **27** 092001
[69] Liscio A, Kouroupis-Agalou K, Betriu X D, Kovtun A, Treossi E, Pugno N M, De Luca G, Giorgini L and Palermo V 2017 Evolution of the size and shape of 2D nanosheets during ultrasonic fragmentation *2D Mater.* **4** 25017
[70] Marchese Robinson R L *et al* 2016 How should the completeness and quality of curated nanomaterial data be evaluated? *Nanoscale* **8** 9919–43
[71] Feliu N, Walter M V, Montañez M I, Kunzmann A, Hult A, Nyström A, Malkoch M and Fadeel B 2012 Stability and biocompatibility of a library of polyester dendrimers in comparison to polyamidoamine dendrimers *Biomaterials* **33** 1970–81